Development of a Hollow-Core Fiberoptic Microneedle Device for the Treatment of Invasive Bladder Cancer

Robert Lyle Hood

Thesis submitted to the faculty of Virginia Polytechnic Institute and State University in partial
fulfillment of the requirements for the degree of

Masters of Science
In
Biomedical Engineering

Christopher Rylander
Nichole Rylander
David Grant
John Robertson

August 11th, 2011 – ICTAS 310
Blacksburg, VA

Keywords: Microneedle, Microfluidic Device, Biomimetic Infusion, Convection-Enhanced Diffusion, Biotransport, Carbon Nanohorn

Development of a Hollow-Core Fiberoptic Microneedle Device for the Treatment of Invasive Bladder Cancer

Robert Lyle Hood

Abstract

The hydraulic resistance characterization manuscript chronicles the early development of the hollow-core fiberoptic microneedle device (FMD). The study determined that for straight tubing with an inner bore of 150 μm and a length greater than 50 mm long, Poiseuille's Law was shown to be accurate within 12% of experimental data for the pressure range of 69-517 kPa. Comparison between different needle design geometries indicated that tip diameters <55 μm cause a significant increase in hydraulic resistance. Tubing length should be kept to a minimum and tip diameter should be kept above this threshold to reduce overall hydraulic resistance.

The bladder treatment study describes the fabrication and testing of the FMD for treatment of invasive urothelial cell carcinomas (UCCs). Experiments investigating the fluid dispersal of single-walled carbon nanohorns (SWNHs) in the wall of inflated, healthy *ex vivo* bladders demonstrated that perfusion of 2 cm^2 on the bladder wall's surface can be achieved with a 5 minute infusion at 50 μL/min. Irradiation of the SWNH perfused bladder wall tissue with a free space, 1064 nm laser at an irradiance of 0.95 W/cm^2 for 40 seconds yielded a 480% temperature increase relative to similar irradiation of a non-infused control. Co-delivery experiments demonstrated both SWNH and light delivery though a single hollow-core fiber to heat the bladder wall 33 ^0C with an irradiance of 400 W/cm^2, demonstrating that the FMD can be used to achieve hyperthermia-based therapeutic effects via interstitial irradiation.

Keywords: Hollow-core microneedle, simultaneous co-delivery, photothermal therapy

Acknowledgements

I would like to acknowledge my advisors, colleagues, and friends that helped guide me through developing this project from concept to prototype. I would like to thank Dr. Chris Rylander and Dr. John Robertson for their mentorship, advice, and encouragement throughout my time in the Biotransport and Optics Laboratory. In addition, I would like to recognize that the faithfulness and support of my God, family and friends made my success possible, with the most notable contributions from the last group by Goldie Darr, William Vogt, Amanda Rodgers, and William Carswell.

TABLE OF CONTENTS

LIST OF FIGURES

LIST OF TABLES

Chapter 1: **Introduction**

1.1 Introduction to the Hollow-Core Fiberoptic Microneedle Device

In recent years, developments in microscale fabrication have enabled the creation of needles on the scale of micrometers. These “microneedles” can be created out of a variety of materials such as polymers, metals, or glass, and are utilized to facilitate highly accurate small volume fluid delivery with minimal tissue disruption. Studies have shown that needle diameter and insertion force are primary determinants of patient pain caused by transdermal injection [1-3]. The small diameter of these microneedles reduces the invasiveness and patient sensation associated with their clinical use. The potential presented by these microneedles for therapeutic and diagnostic applications has led to a significant investment of research attention.

One of the first therapeutic applications utilizing microneedles was increasing the effectiveness of transdermal drug delivery patches by increasing skin permeability with slight penetration (< 1 mm) [4]. Other applications involved using microneedles as electrodes to measure electrical potentials or cause electroporation in tissue [5-7] Other groups have successfully utilized these needles for intrascleral delivery of therapeutic agents and to inoculate patients against disease [8, 9]. Solid, biodegradable polymer microneedles containing dissolved pharmaceuticals have been developed for time-delayed drug release [10-12]. Due to the lessened patient discomfort associated with microneedles, they have been developed for use in patients with conditions that require frequent infusions, such as diabetics [13]. However, the small diameters of microneedles make delivery of larger volumes difficult. To bypass this difficulty, parallel arrays of microneedles can be utilized. Early developers of this design successfully delivered sufficient insulin to lower glucose levels in diabetic rats [13, 14]. In a more refined variant of the parallel

array design, one group developed a microneedle-based transdermal patch device that allowed for the active dispensation of insulin [15]. Microneedles are continuing to receive a great amount of research attention, with new designs being applied to novel applications in many diverse fields.

The research described focuses on fluid flow characterization through a novel type of hollow-core silica microneedle that allows for several millimeters of tissue penetration and co-localized light and fluid delivery. These microneedles can be made from silica capillary tubing capable of guiding laser light. A device with this dual capability can be readily adapted to several applications, such as treatment of non-superficial, focal cancers by delivery of exogenous chromophores and laser irradiation from the same probe. Cosmetic laser-based applications such as body contouring may also benefit from this technology through simultaneous fat liquefaction and removal from sensitive areas such as the face.

1.2 Introduction to FMD Treatment of Invasive Urothelial Cell Carcinoma

Urinary bladder cancer is the fourth most common non-cutaneous malignancy of humans in the United States with approximately 71,000 new cases diagnosed and 15,000 deaths in 2010 [16]. Urothelial cell carcinoma (UCC, synonymous with transitional cell carcinoma) accounts for approximately 90% of all bladder cancers. Over 30% of UCCs are at an advanced clinical stage when diagnosed, with penetration of tumor cells into the muscularis propia (stages 3 and 4), serosa (stage 4 only), and metastasis to surrounding organs [17-19]. Radical cystectomy of invasive UCC is the current standard treatment, but its use frequently results in significant post-operative complications and poor patient quality of life [20]. This treatment typically requires

removal of the bladder, nearby lymph nodes, and part of the urethra in both sexes; the prostate, seminal vesicles, and vas deferens in men; and the ovaries, Fallopian tubes, and part of the vagina in women [20-22]. This treatment often results in sexual dysfunction, electrolyte imbalances, bone loss, and deterioration of the kidneys [23, 24]. Patients are faced with poor quality-of-life, bleak prognosis, and low survival rate (30-50% at 5 years post diagnosis) [17].

Although patient outcomes for advanced stage, invasive bladder cancers are statistically poor, patient outcomes for early stage (stages 0-1) bladder cancers are relatively hopeful [25-27]. The primary treatment for such early lesions is transurethral resection of the bladder (TURB) followed by chemotherapy [27-32]. One of the original laser-based alternatives for treatment of superficial bladder tumors was Nd:YAG laser photoablation at a 1064 nm wavelength. Unfortunately, laser energy delivered at this wavelength is damaging to underlying tissues [25, 28, 33, 34]. Nd:YAG-based treatments were succeeded by the Ho:YAG laser (2.1 μm wavelength) for photothermal treatment of superficial bladder cancers, which has become widely utilized. Several studies have shown that treatment with the Ho:YAG laser is safe, effective, and associated with rapid patient recovery, indicating it is a viable alternative to standard TURB or electrocautery for treating early stage bladder cancer [26-28, 34].

While effective for superficial tumors, Ho:YAG laser treatment has proven ineffective for invasive, late stage bladder tumors due to insufficient light penetration into the tumor mass [26, 28, 34-36]. Light at a wavelength of 2.1 μm penetrates bladder tissue approximately 0.5 mm, which is insufficient to treat late-stage tumors that invade the muscular and serosal layers 2-4 mm into the bladder wall [19, 28]. Inadequate delivery and heating of deep tumor volumes

results in generation of poorly defined lesion boundaries and a high likelihood of tumor re-growth, recurrence, necrosis, and possible perforation of the bladder wall [24, 37].

Recognizing the limitations of current laser-based treatments for bladder cancer, we have invented a fiberoptic microneedle device (FMD) that allows significantly enhanced laser light penetration to desired target tissue depths and selective amplification of thermal dose through introduction of exogenous chromophores such as nanoparticles. This device is comprised of one or more hollow-core fiberoptics (HCFs) capable of co-delivering fluids and light. Light conduction is permitted in the annular wall of the silica fiber, and fluid is infused through the hollow central bore. The tips of the fibers can be angle-polished to a sharp, <100 μm microneedle tip, which can penetrate a neoplasm's exterior and deliver treatment to invasive depths. The FMD also includes the necessary components to couple light (from a free-space or fiberoptic source) and fluid (from a reservoir and/or pumping apparatus) into the HCF.

For treatment of invasive UCCs, we envision that the one or more HCFs would be guided into the bladder via the working channel of a cystoscope and placed against a tumor located in the bladder urothelium. Mechanical actuation will cause the HCFs to slide through the channel and penetrate the bladder to a final placement at desirable target positions within an invasive UCC. Delivery of exogenous chromophores to specific tissue regions will allow for a localized, targeted treatment and preservation of surrounding healthy tissues. Laser energy emitted from the microneedle tip will be selectively absorbed by the SWNHs in a target tissue's interstitial space. This should enable significantly reduced unwanted collateral healthy tissue damage while maximizing energy delivery to tumor tissue.

1.3 Project Overview

The focus of this project was to develop the FMD as a technology suitable for the treatment of invasive cancers. The three major advantages offered by this system are 1) the microneedle can penetrate the exterior of the tissue to deliver therapy interstitially throughout the thickness of a tumor; 2) the FMD can be used to present chemotherapy, image-enhancing molecules, photosensitizers, or any other clinical molecule that can be presented as a fluidic solution to an interstitial space; and 3) the FMD can deliver light interstitially for light-based therapies or collect light for imaging. As the microneedle is made from hollow fiberoptics, the initial challenge to development was the characterization of fluid flow through the fiber and microneedle tip. Once the fluid delivery was understood, invasive bladder cancer was the first application the FMD was customized to treat. The research described in the manuscript below addresses the fluid delivery characterization, the design modifications introduced to create a FMD applicable to bladder cancer treatment, and experimental testing of the resulting device as a potential therapeutic device.

Chapter 2: **Effects of Microneedle Design Parameters on Flow Rate and Hydraulic Resistance**

2.1 Abstract

Microneedles have been an expanding medical technology in recent years due to their ability to penetrate tissue and deliver therapy with minimal invasiveness and patient discomfort. Variations in design have allowed for enhanced fluid delivery, biopsy collection, and the measurement of electric potentials. Our novel microneedle design attempts to combine many of these functions into a single length of silica tubing capable of both light and fluid delivery terminating in a sharp tip of less than 100 microns in diameter. This manuscript focuses on the fluid flow aspects of the design, characterizing the contributions to hydraulic resistance from the geometric parameters of the microneedles. Experiments consisted of measuring the volumetric flow rate of de-ionized water at set pressures (ranging from 69-621 kPa) through a relevant range of tubing lengths, needle lengths, and needle tip diameters. Data analysis showed that the silica tubing (~150 micron bore diameter) adhered to within ±5% of the theoretical prediction by Poiseuille's Law describing laminar internal pipe flow at Reynolds numbers less than 700. High hydraulic resistance within the microneedles correlated with decreasing tip diameter. The hydraulic resistance offered by the silica tubing preceding the microneedle taper was approximately 1-2 orders of magnitude less per unit length, but remained the dominating resistance in most experiments as the tubing length was >30 mm. These findings will be incorporated into future design permutations to produce a microneedle capable of both efficient fluid transfer and light delivery.

2.2 Introduction

In recent years, developments in microscale fabrication have enabled the creation of needles on the scale of micrometers. These “microneedles” can be created out of a variety of materials such as polymers, metals, or glass, and are utilized to facilitate highly accurate small volume fluid delivery with minimal tissue disruption. Studies have shown that needle diameter and insertion force are primary determinants of patient pain caused by transdermal injection [1-3]. The small diameter of these microneedles reduces the invasiveness and patient sensation associated with their clinical use. The potential presented by these microneedles for therapeutic and diagnostic applications has led to a significant investment of research attention.

One of the first therapeutic applications utilizing microneedles was increasing the effectiveness of transdermal drug delivery patches by increasing skin permeability with slight penetration (< 1 mm) [4]. Other applications involved using microneedles as electrodes to measure electrical potentials or cause electroporation in tissue [5-7] Other groups have successfully utilized these needles for intrascleral delivery of therapeutic agents and to inoculate patients against disease [8, 9]. Solid, biodegradable polymer microneedles containing dissolved pharmaceuticals have been developed for time-delayed drug release [10-12]. Due to the lessened patient discomfort associated with microneedles, they have been developed for use in patients with conditions that require frequent infusions, such as diabetics [13]. However, the small diameters of microneedles make delivery of larger volumes difficult. To bypass this difficulty, parallel arrays of microneedles can be utilized. Early developers of this design successfully delivered sufficient insulin to lower glucose levels in diabetic rats [13, 14]. In a more refined variant of the parallel array design, one group developed a microneedle-based transdermal patch device that allowed

for the active dispensation of insulin [15]. Microneedles are continuing to receive a great amount of research attention, with new designs being applied to novel applications in many diverse fields.

The research described in this paper focuses on fluid flow characterization through a novel type of hollow-core silica microneedle that allows for several millimeters of tissue penetration and co-localized light and fluid delivery. These microneedles can be made from silica capillary tubing capable of guiding laser light. A device with this dual capability can be readily adapted to several applications, such as treatment of non-superficial, focal cancers by delivery of exogenous chromophores and laser irradiation from the same probe. Cosmetic laser-based applications such as body contouring may also benefit from this technology through simultaneous fat liquefaction and removal from sensitive areas such as the face.

Our fiberoptic microneedle design incorporates tubing of an inner bore diameter of 150±1 μm with a fabricated microneedle tip with diameter ranging between 20-100 μm. The sharpened tip is necessary to lower the force required for penetration and thereby safeguard the structural integrity of the needle, in addition to minimizing patient discomfort [3, 38]. Our design is biomimetic, as the mosquito's proboscis is of similar proportions and is able to painlessly penetrate millimeters into an animal's skin to extract blood [39]. These microneedles can be incorporated into many applications that require accurate localized delivery of small fluid volumes. The experiments performed in this study characterized the fluid flow properties of this transformative microneedle design so that it may be easily integrated into devices for a range of

applications. More specifically, the experiments sought to determine the most important factors contributing to the hydraulic resistance to fluid flow in this design.

2.3 Methods

a) Manufacturing Process for Hollow-Core Microneedles

Commercially available flexible fused silica capillary tubing was utilized in the characterization of the fluid properties for our design. The fused silica capillary tubing had an outer diameter of 363±4 μm , an inner diameter of 150±1 μm, and a coating thickness of 40 μm (Polymicro Technologies, Phoenix, AZ). The microneedle fabrication method outlined below is similar to that described in a previous publication by this group for solid-core microneedles [38]. To begin the fabrication process, the protective polyimide jacket (40 μm coating) was removed from the silica tubing through soaking in a warmed sulfuric acid (~130^{o} C) bath for 15 minutes. The silica was drawn into a microneedle geometry by simultaneously heating the tubing with a CO_2 laser (wavelength, λ = 10.6 μm) to silica's melting temperature (~1650^{o}C) while stretching it with a linear stage providing uniaxial tension (~0.2 - 1 mm/s, manually translated). The drawing speed was intentionally varied to fabricate tip diameters ranging from 30-75 μm. Microscope images of several representative hollow-core microneedles are shown in Figure 1.

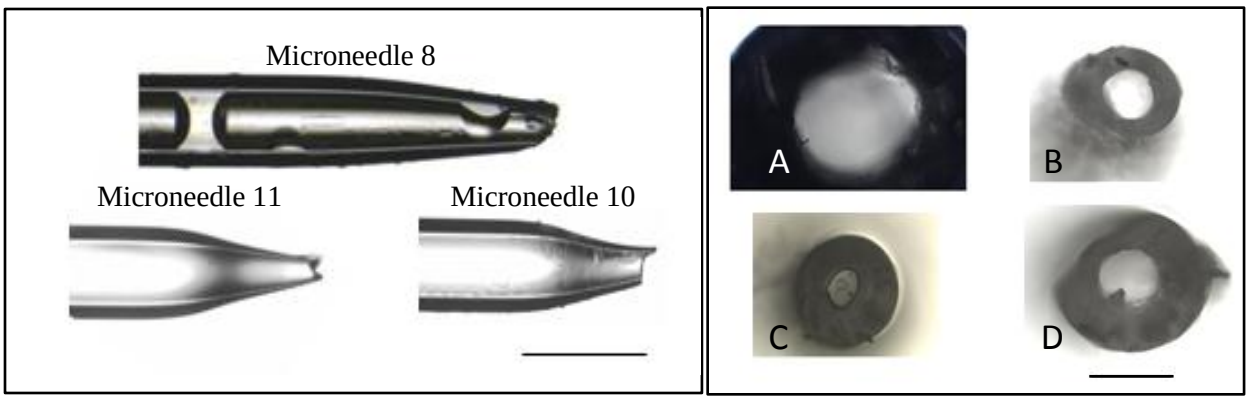

Figure 1: Left) Three sample hollow-core microneedles. The scale bar represents 500 µm. Water within the needle's bore can be seen in the image of microneedle 8. Right) *En face* images of the tips of a) flat-cleaved tubing b) needle 10 c) needle 11 d) needle 113. Scale bar represents 100 µm.

b) Hydraulic Circuit Analysis

In order to determine the most important factors contributing to hydraulic resistance, an experimental approach utilizing two successive stages was developed. Stage I consisted of characterizing the hydraulic resistance of the tubing that would precede the microneedle, while Stage II sought to characterize the resistance of the microneedle itself. This approach can be modeled via hydraulic circuit analysis as outlined by Kirby [40]. In Stage I, the hydraulic resistance of the flat cleaved tubing (150 µm inner diameter) was tested. The experiment consisted of using pressured CO_2 to drive deionized water through the tubing into atmospheric pressure. Laminar internal flow through a pipe is described by Poiseuille's Law as

$$R_{TUBE} = \frac{\Delta P}{Q} = \frac{128\,\mu L}{\pi D^4} \quad (1)$$

where R_{TUBE} is the hydraulic resistance (Pa·s/µL), ΔP is the pressure difference (Pa), Q is the volumetric flow rate (µL/s or mm^3/s), D is the pipe's diameter (mm), µ is the dynamic viscosity

($N \cdot s/m^2$), and L is the length of the pipe or tube (mm). The hydraulic circuit analytical model of a tube with a single (lumped) resistance is representated in Figure 2. To facilitate better physical understanding and ease of calculation, the units for hydraulic resistance were input pressure divided by the measured volumetric flowrate (Pa·s/μL) and were reported as such in this manuscript.

In Stage II, the hydraulic resistance of a length of tubing with an attached microneedle was tested via the same method as Stage I. As the resistance provided by the initial tubing (R_{TUBE}) would be understood after the completion of Stage I, the series resistance provided by the microneedle (R_{NEEDLE}) could be isolated and quantified (depicted in Figure 3). The total hydraulic resistance can then be described mathematically by

$$R_{TUBE} + R_{NEEDLE} = \frac{\Delta P}{Q} = R_{TOTAL} \quad (2)$$

where R_{TUBE} describes the resistance to flow due to the tubing length preceding the microneedle, R_{NEEDLE} is the resistance provided by the microneedle, and R_{TOTAL} is the total resistance. Assuming these resistances are linear and ideal (no capacitance or inductance), this equation should describe the ideal case of flow defined by viscous forces alone (limited inertial effects) through the microneedle design.

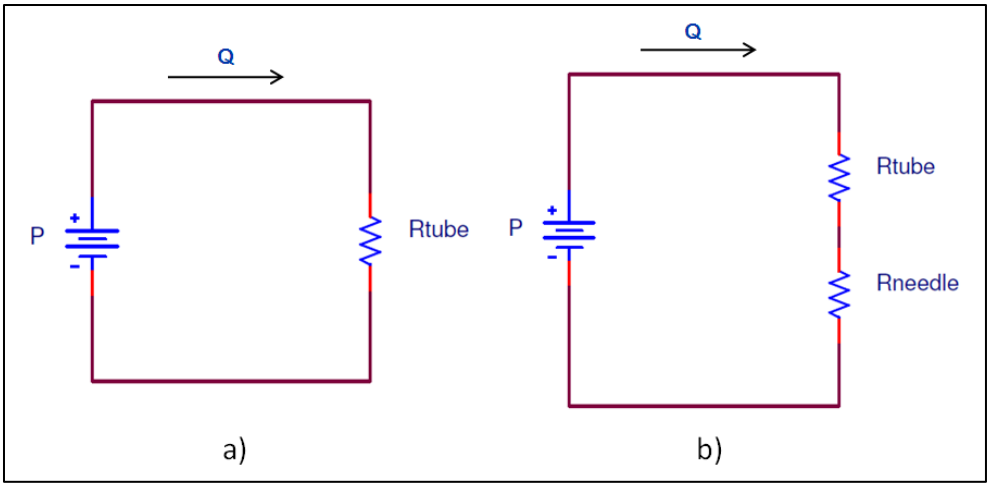

Figure 2: Hydraulic circuit analytical model representation of resistance in a) a capillary tube (Stage I) and b) tube with a microneedle tip (Stage II).

To correctly interpret results obtained via this experimental model, an understanding of the flow turbulence in the tubing and microneedles was important. The dimensionless Reynolds number describes this effect, and is calculated for internal pipe flow by:

$$\mathrm{Re} = \frac{\mathrm{QD}}{\upsilon \mathrm{A}} \tag{3}$$

where Re is the Reynolds number, ν is the kinematic viscosity (m^2/s), and A is the cross-sectional area of the pipe (m^2). For Stage II, the Reynolds number increased along the length of the needle towards the tip as the diameter decreased.

c) Hydraulic Resistance Experiments

A simple fluid deployment device (FDD) was fabricated as shown in Figure 3 to allow for variable input pressures and have negligible hydraulic resistance relative to the tubing or microneedles being tested. The individual components of the device consisted of brass and stainless steel piping, ball valves, inline filter (10 micron in-line filter, FloLok®, Twinsburg,

OH), a Luer Lock adapter (1/4 NPT male to Luer Lock, Ellsworth Adhesives, Germantown, WI), and an 18G hypodermic needle (0.838 mm inner diameter). The filter minimized clogging of the needles, and the adapter enabled rapid removal and replacement of different tubing sections and microneedles. The volumetric flow rate of water through the FDD was measured by timed collection and weighing of DI water exiting the FDD. The resistance through the FDD alone (without tubing or microneedle attached) was calculated to be between 2 and 3 orders of magnitude less than the test resistances, which was further observed experimentally. This evidence indicated that the FDD presented an insignificant series resistance that would be constant across all experiments. The different lengths of flat cleaved tubing and microneedle-tipped tubing were epoxy-bonded into 18 gauge hypodermic needles (1.067 mm inner diameter) for interface with the FDD. Excess tubing length extended through the Lure-Lok adapter into the setup, ensuring that the syringe needle did not contribute to the hydraulic resistance of the system. The bonding epoxy served to both fix the tubing in the hypodermic needle and prevent potential leaks. Any leakage from the device or hypodermic immediately invalidated the relevant experiment.

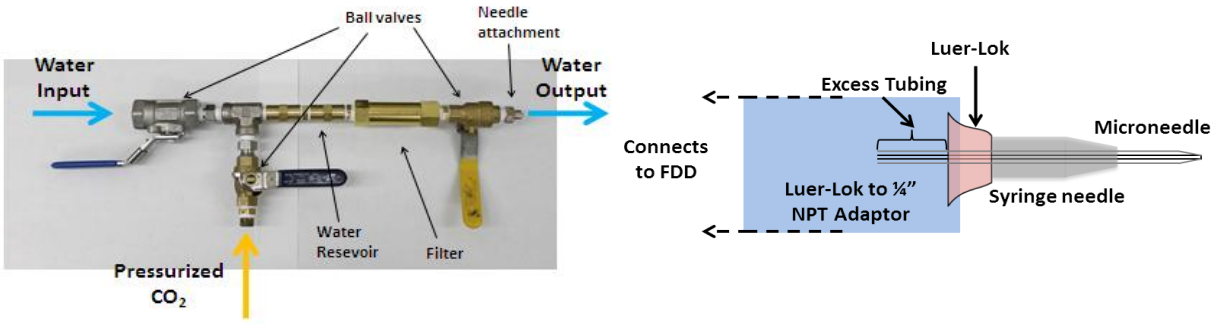

Figure 3: The left image shows the fluid deployment device (FDD) with specific components labeled. The right image shows a schematic of the microneedle coupling. The microneedle is epoxy-bonded into an 18G syringe needle, which couples to a Luer-Lok to ¼" NPT adaptor at the distal end of the FDD.

The experimental preparation was identical for Stages I-II. De-ionized water was added to the FDD (10-15 mL) and any air was bled from the system. Next, the FDD was pressurized to the desired experimental level by a CO_2 tank and regulator setup. For both stages, the weight of a small beaker (50 mL volume) was tared on an analytical balance with 0.1 mg (or 0.1 µL of water) accuracy. The beaker was used to capture flow through the test resistance. Once the empty beaker was in position, the valve directly adjacent to the test resistance was opened, allowing fluid flow through the resistance and into the beaker.

Exiting water was captured for a set time (30 s) and then immediately taken to the balance for weighing to determine the fluid flow rate. While evaporation was insignificant (around 0.8 µL/min) relative to total captured volume (2-5 mL), rapidly weighing the beaker immediately after timed capture ensured that the effect of evaporative water loss was minimized. The experimental test pressures used for both stages ranged from 69 to 621 kPa (10-90 psi). For

Stage I, 6 different tubing lengths were tested at each of the experimental pressures 3 or more times. For Stage 2, 15 different microneedles with different tubing length precursors were tested 5 or more times at each experimental pressure.

Both partial and complete clogging of the needles was observed infrequently during the Stage II experiments. Microneedles were observed under a microscope prior to experimentation to detect any flow obstruction. The experiments were conducted on each microneedle with incrementally increasing pressure, so any sudden drop in flow rate caused by flow obstruction was immediately evident. Any microneedle observed to have an obstruction was immediately removed from testing and cleared through deployment of a solvent (ethanol or acetone) through the needle. The previous data was discarded and the relevant experiments repeated for the cleared microneedle.

2.4 Results

a) Stage I Experimental Results

Flow rate was measured through different lengths of flat-cleaved tubing to measure the hydraulic resistance (R_{TUBE}). By conducting the experiments over a range of input pressures, graphs of flow rate versus pressure were generated and are presented in Figure 4.

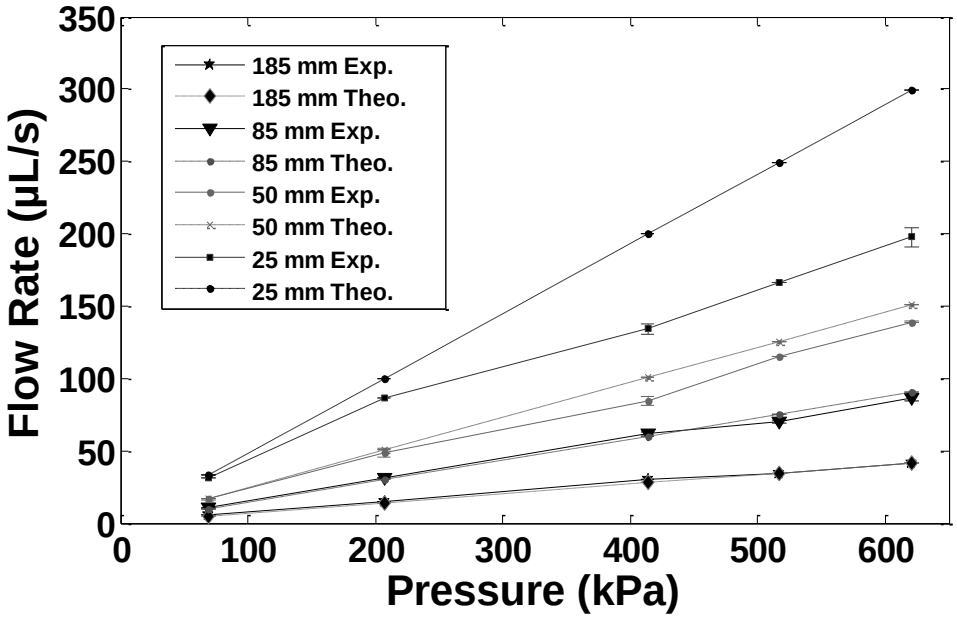

Figure 4: Graph of pressure versus volumetric flow rate for different lengths of straight tubing in Stage I. Both experimental data and theoretical values predicted by Poiseuille's Law are shown. Experiments were conducted at N=5 for each length of tubing.

Using the experimental data, resistance values were calculated for the different tubing lengths and compared to resistances predicted by Poiseuille's Law. Calculation of the tubing resistance from the pressure and flow rate data using Eqn. (1) yielded the results shown in Table 1.

Table 1: Resistance values calculated from Stage I experiments compared to the theoretically predicted values provided by Poiseuille's Law. Resistance units are in Pa·s/µL.

Tube Length	185 mm	125 mm	85 mm	70 mm	50 mm	25 mm
Experimental R_{TUBE}	15647	10764	7305	6010	4577	3439
Poiseuille R_{TUBE}	14926	10085	6858	5406	4115	2072
% Difference	4.83%	6.72%	6.51%	11.2%	11.2%	66.0%

b) Stage II Experimental Results

Graphs of pressure versus volumetric flow rate for tubing with attached microneedles are provided in Figure 5. The selected microneedles represent the range of volumetric flow rates measured. The total hydraulic resistance of tubing with microneedle tips was calculated from this experimental data.

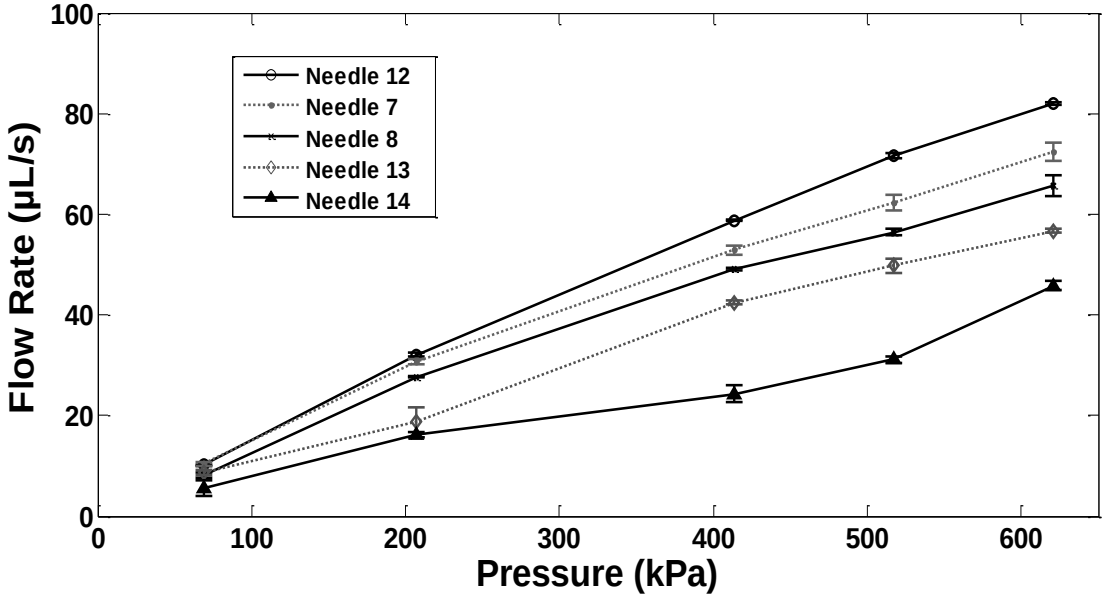

Figure 5: Measured flow rate versus pressure for tubes and microneedles. Error bars are included on all points, but do not extend outside the marker in some cases. Experiments were conducted with N=5 for each microneedle.

The hydraulic resistance associated specifically with the microneedle tip could be determined from Eqn. (1) ($R_{NEEDLE} = R_{TOTAL} - R_{TUBE}$), where R_{TUBE} is theoretically predicted using Poiseuille's Law. For Microneedles 1-15, the needle resistance ranged from 990to 8230 Pa·s/µL at 207 kPa. High resistance correlated moderately with decreasing tip size.

Geometric parameters of fabricated microneedles (including length and taper angle) were described previously be this group [38]. The microneedles generally resembled straight-sided cones with linearly decreasing cross-sections. Needle measurements were taken from images recorded with a Leica DMIL LED light microscope (Leica Microsystems, Wetzlar, Germany) on the brightfield setting. Both sideview and *en face* images were measured and compared to ensure accuracy as shown previously in Figure 1. The geometric parameters and experimentally measured resistances for the different microneedles are shown in Table 2.

Table 2: Geometric parameters and the experimentally measured resistances of the fourteen microneedles tested.

Needle #	Tube Length (mm)	Needle Length (μm)	Tip Diameter (μm)	Taper Angle (degrees)	R_{Needle} @ 207 kPa (Pa·s/μL)
1	70	410	75	5.2^o	990
2	30.5	496	59.7	5.2^o	1100
3	77.5	1015	68.3	2.3^o	1180
4	83	1116	40	2.8^o	1800
5	60.5	307	75.3	6.9^o	1860
6	69.5	683	61.5	3.7^o	1920
7	68	1152	66	2.1^o	2040
8	77	516	70	4.4^o	2110
9	69.5	997	71	2.3^o	2270
10	56.5	698	38.1	4.6^o	3280
11	60	701	38	5.5^o	4130
12	46.5	541	40	5.8^o	4880
13	38	634	50	4.5^o	5690
14	58	724	30	4.7^o	8230

2.5 Discussion

Based on the experiments determining the flow rate through the hollow tubes, we calculated the Reynolds numbers for each experiment to determine the validity of Poiseuille's Law as a model for our tubing. The range of Reynolds numbers for the Stage I experiments varied from 50 to

1675, indicating that flow through the shortest tubing lengths at the highest pressures exhibited both viscous and inertial traits. As our Poiseuille's Law model is based on ideal laminar pipe flow, its prediction of the hydraulic resistance should be less than that observed experimentally. As Table 1 indicates, Poiseuille's Law was not an accurate predictor (>5% deviation) for the flow resistance through tubing (without a microneedle tip) at Reynolds numbers greater than 700. In contrast, the high resistance provided by microneedles kept the flow in the tubing preceding the needle within a lower Reynolds number range ($100<Re<500$) in all of the Stage II experiments, allowing Poiseuille's Law to be an accurate model for the tubing.

For the Stage II experiments, the hydraulic resistance for the microneedles increased significantly with increased pressure, with an average increase of 33% from 69 to 620 kPa. This was likely due to increased turbulence in the fluid flow near the sharpest point of the needle, as the Reynolds numbers at the microneedle tips approached 3600 (well above the onset of transitional flow at Re = 2100) for the smallest tip diameter (30 μm) at the highest pressure (621 kPa) [41]. Hydraulic resistance at 207 kPa was chosen as the metric with which to compare different microneedles, as flow at 69 kPa was not continuous (dripping) for some of the higher resistance needles and pressures greater than 207 kPa exhibited increasingly transitional flow. In addition, Reynolds numbers calculated for the tubing sections at this pressure in Stage II fell within the range of 50-500 Pa·s/μL, indicating laminar flow and adherence to Poiseuille's Law. Comparing the hydraulic resistances at 207 kPa allowed for better isolation of the direct effects of geometry on fluid flow.

Entrance length for each tubing and microneedle were calculated to determine its effects. An approximate value for entrance length of developing flow can be calculated with Eqn. 4

$$\left(\frac{Entrance\ Length}{Hydraulic\ Diameter}\right)_{Laminar\ Flow} = 0.05\ \mathrm{Re} \qquad (4)$$

which relates the entrance length, hydraulic diameter, and Reynolds number for laminar internal pipe flow [42]. For the Stage I experiments, the longest entrance length (25 mm tube, 620 kPa) was found to be 12.7 mm. Using flow analysis outlined by Zahn et al., the pressure drop along this entrance length was found to be ~13 % of the total pressure drop, suggesting entrance effects significantly contributed to the discrepancies between Poiseuille's Law predictions and the experimental measurements in the Stage I experiments [43]. However, due to the higher overall resistance added by the microneedle tips in Stage II and the chosen comparison pressure of 207 kPa, the longest entrance length among the microneedles was found to be 3.7 mm. Since tubing with attached microneedles were $\geq$ 25 mm in length, these calculations suggest that the entrance effects for the Stage II experiments were negligible as the flow reaches a fully-developed state preceding the microneedles, thus supporting the use of Poiseuille's Law as a model for the straight tubing portion of the microneedle.

Data gathered in this study was consistent with the established literature on the flow behavior in conically-tapered microneedles in that small forces (such as capillarity) did not influence flow behavior significantly [44, 45]. As hydraulic resistance was most sensitive to tip diameter, future design iterations may include a conically beveled microneedle tip. Fortunately, the data gathered in these experiments should also predict flow from a beveled tip, as the diameter of the closed tube before the spread of the bevel should behave similarly to the flat microneedle tips from this study.

Poiseuille's Law predicts a tubing hydraulic resistance of 80.7 Pa·s/µL per mm for the straight tubing used in these experiments. Thus, the total tubing resistance theoretically varies from 2100 to 15000 for lengths between 25 and 185 mm. The microneedle hydraulic resistance values measured in Stage II ranged from 990 to 8230 Pa·s/µL at 207 kPa. This finding indicates that fluid flow through the tubing should be kept at a minimum length as this design continues in development, an important concept as some tubing length may be necessary for successful coupling of both light and fluid into the same microneedle.

Hydraulic resistance tended to be highest for needles with small tip diameters. This is illustrated in Figure 5. The average resistance for needles with tip diameters between 30-55 µm was approximately 4270±2260 Pa·s/µL, while average resistance for needles between 55-90 µm was 1680±510 Pa·s/µL. As can be seen in Figure 5, the resistance for tip diameters less than 55 µm tends to be higher, but the data has significantly more spread. This data spread can be attributable to the greater influence of surface irregularities on the inner bore surface of the needle or the increased flow alteration due to minor clogging. The microneedles with <55 µm tip diameters were shown to be of significantly greater in hydraulic resistance than the microneedles with >55 µm by a Welch's t-test with 95% confidence**.**

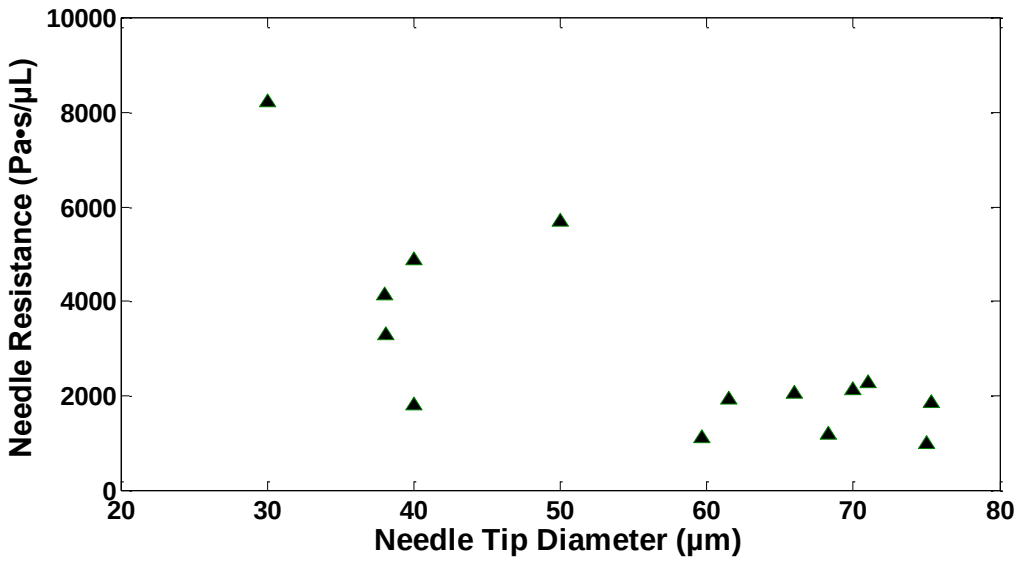

Figure 5: Hydraulic resistance of the fourteen microneedles plotted against their tip diameters.

This paper presents a transformative microneedle design capable of co-delivering fluid and light several millimeters beneath a tissue's surface. Parallel work to characterize the light delivery capacity of these microneedles is currently underway. This manuscript focuses on experiments investigating the needles' hydraulic resistance to fluid flow. For straight tubing with an inner bore of 150 µm and a length greater than 50 mm long, Poiseuille's Law was shown to be accurate within 12% of experimental data for the pressure range of 69-517 kPa. This silica tubing was also shown to have similar hydraulic resistance to microneedles fabricated from the tubing through our proprietary method. Comparison between different needle design geometries indicated that tip diameters <55 µm cause a significant increase in hydraulic resistance. Tubing length should be kept to a minimum and tip diameter should be increased to the largest possible size to reduce overall resistance. Future investigations should also consider the resistance to flow by the tissue at the microneedle tip, as this is important for future clinical translation. Similar experiments with these microneedles *in vivo* will accelerate translation of their use to clinical

practice. To achieve reasonably low hydraulic resistances in clinical practice, parallel arrays of these microneedles could deliver fluids simultaneously at lower pressures. This concept has been demonstrated by other groups, and could be easily incorporated into our design [13, 15].

Chapter 3: **A Novel Hollow-Core Fiberoptic Microneedle Treatment for Invasive Urothelial Cell Carcinomas**

3.1 Abstract

Background and Objectives: Laser-based therapies for urothelial cell carcinoma (UCC) are a promising alternative to surgical resection. However, these therapies are currently limited to photothermal ablation of superficial tumors using shallow-penetration laser sources such as Ho:YAG. A fiberoptic microneedle device (FMD), developed in this study, overcomes this obstacle by penetrating the bladder mucosa and muscularis to co-deliver exogenous photoabsorbers and light interstitially, potentially increasing the spatial control of treatment. The goal of this study was demonstration of the FMD's potential to treat invasive UCCs by co-delivering photoabsorbing single-walled carbon nanohorns (SWNHs) and 1064 nm wavelength light into healthy, *ex vivo* bladder tissue.

Materials and Methods: SWNHs in aqueous solution were infused through the FMD into the wall of healthy, inflated *ex vivo* bladders to demonstrate fluid delivery and determine the rate of nanoparticle dispersal across the bladder's serosa. Formalin-fixed inflated and uninflated bladders were sectioned and studied after SWNH infusion to determine the depth of nanoparticle penetration through the wall's thickness. SWNH perfused bladder regions were irradiated with a free-space 1064 nm laser while monitoring surface temperature with a thermal camera in order to determine the SWNH-mediated temperature increase. A FMD allowing co-delivery of 1064 nm laser light and SWNHs in solution through a single hollow-core microneedle was fabricated. Experiments utilizing this device to deliver both SWNH solution and laser energy were conducted to demonstrate co-delivery in the bladder wall.

Results: SWNHs in solution at a concentration of 0.05 mg/mL were infused at 50 µL/min into the walls of healthy, inflated *ex vivo* bladders resulting in an average rate of expansion across the bladder wall of 0.36 ± 0.08 cm^2/min. Infusion into inflated bladders exhibited dispersal throughout the thickness of the bladder wall after 5 minutes at 50 µL/min. Irradiation of bladder tissue perfused with SWNHs with 1064 nm, continuous wave laser light at 0.95 W/cm^2 exhibited a 480% increase in temperature over a 40 second exposure period compared to non-perfused bladder tissue. An FMD prototype allowing co-delivery through a single hollow-core fiber was successfully fabricated and utilized to deliver nanoparticles and laser energy to bladder tissue for a maximum temperature increase of 33 °C at an irradiance of 400 W/cm^2 over 40 seconds.

Conclusions: We have designed and fabricated a new device platform for co-delivery in bladder tissue with the potential for photothermal treatment of invasive UCCs. Preliminary experiments demonstrated that temperatures causing hyperthermic cell death could be attained with co-delivery of both SWNHs and laser light through FMDs. Additional experiments are necessary to determine the safety and therapeutic efficacy of this technique.

3.2 Introduction

Urinary bladder cancer is the fourth most common non-cutaneous malignancy of humans in the United States with approximately 71,000 new cases diagnosed and 15,000 deaths in 2010 [16]. Urothelial cell carcinoma (UCC, synonymous with transitional cell carcinoma) accounts for approximately 90% of all bladder cancers. Over 30% of UCCs are at an advanced clinical stage

when diagnosed, with penetration of tumor cells into the muscularis propia (stages 3 and 4), serosa (stage 4 only), and metastasis to surrounding organs [17-19]. Radical cystectomy of invasive UCC is the current standard treatment, but its use frequently results in significant post-operative complications and poor patient quality of life [20]. This treatment typically requires removal of the bladder, nearby lymph nodes, and part of the urethra in both sexes; the prostate, seminal vesicles, and vas deferens in men; and the ovaries, Fallopian tubes, and part of the vagina in women [20-22]. This treatment often results in sexual dysfunction, electrolyte imbalances, bone loss, and deterioration of the kidneys [23, 24]. Patients are faced with poor quality-of-life, bleak prognosis, and low survival rate (30-50% at 5 years post diagnosis) [17].

Although patient outcomes for advanced stage, invasive bladder cancers are statistically poor, patient outcomes for early stage (stages 0-1) bladder cancers are relatively hopeful [25-27]. The primary treatment for such early lesions is transurethral resection of the bladder (TURB) followed by chemotherapy [27-32]. One of the original laser-based alternatives for treatment of superficial bladder tumors was Nd:YAG laser photoablation at a 1064 nm wavelength. Unfortunately, laser energy delivered at this wavelength is damaging to underlying tissues [25, 28, 33, 34]. Nd:YAG-based treatments were succeeded by the Ho:YAG laser (2.1 μm wavelength) for photothermal treatment of superficial bladder cancers, which has become widely utilized. Several studies have shown that treatment with the Ho:YAG laser is safe, effective, and associated with rapid patient recovery, indicating it is a viable alternative to standard TURB or electrocautery for treating early stage bladder cancer [26-28, 34].

While effective for superficial tumors, Ho:YAG laser treatment has proven ineffective for invasive, late stage bladder tumors due to insufficient light penetration into the tumor mass [26, 28, 34-36]. Light at a wavelength of 2.1 μm penetrates bladder tissue approximately 0.5 mm, which is insufficient to treat late-stage tumors that invade the muscular and serosal layers 2-4 mm into the bladder wall [19, 28]. Inadequate delivery and heating of deep tumor volumes results in generation of poorly defined lesion boundaries and a high likelihood of tumor re-growth, recurrence, necrosis, and possible perforation of the bladder wall [24, 37].

Recognizing the limitations of current laser-based treatments for bladder cancer, we have invented a fiberoptic microneedle device (FMD) that allows significantly enhanced laser light penetration to desired target tissue depths and selective amplification of thermal dose through introduction of exogenous chromophores such as nanoparticles. This device is comprised of one or more hollow-core fiberoptics (HCFs) capable of co-delivering fluids and light. Light conduction is permitted in the annular wall of the silica fiber, and fluid is infused through the hollow central bore. The tips of the fibers can be angle-polished to a sharp, <100 μm microneedle tip, which can penetrate a neoplasm's exterior and deliver treatment to invasive depths. The FMD also includes the necessary components to couple light (from a free-space or fiberoptic source) and fluid (from a reservoir and/or pumping apparatus) into the HCF.

For treatment of invasive UCCs, we envision that the one or more HCFs would be guided into the bladder via the working channel of a cystoscope and placed against a tumor located in the bladder urothelium. Mechanical actuation will cause the HCFs to slide through the channel and penetrate the bladder to a final placement at desirable target positions within an invasive UCC.

Delivery of exogenous chromophores to specific tissue regions will allow for a localized, targeted treatment and preservation of surrounding healthy tissues. Laser energy emitted from the microneedle tip will be selectively absorbed by the SWNHs in a target tissue's interstitial space. This should enable significantly reduced unwanted collateral healthy tissue damage while maximizing energy delivery to tumor tissue.

3.3 Methods

a) Bladder Tissue and Experimental Inflation

The *ex vivo* urinary bladders utilized for the experiments in this paper (with the exception of the experiments outlined in 3.3(c) which is explained in that section) were excised from healthy, adult, mixed breed pigs of both sexes purpose-bred for research. The bladders were harvested from freshly sacrificed animals by a veterinarian in the Virginia-Maryland Regional College of Veterinary Medicine. Pigs ranged from approximately 5-10 months of age.

To create a consistent curvature of the bladder wall for the experiments in this study, the *ex vivo* bladders were clamped at the urethra prior to inflation with 500-750 mL of isotonic phosphate buffered saline solution (PBS). Additionally, the exterior of the bladder was moistened at approximately 5 minute intervals with PBS to prevent drying of the serosa that could impact the fluid dispersal properties of the bladder.

b) Dispersal of SWNHs Across the Serosa of the Bladder

SWNHs were synthesized by the Center for Nanophase Materials Sciences at Oak Ridge National Laboratories (Oak Ridge, Tennessee) by previously described methods [46]. The

SWNHs were prepared and suspended in a 1% pluronic solution, as previously described, at a concentration of 0.05 mg/mL [47, 48]. A HCF was affixed within the bore of a 22 gauge needle and attached to a syringe containing SWNH solution by plastic tubing. The HCF was manually inserted with gentle pressure into the serosal layer of an inflated bladder at an angle of approximately 10° from the wall's surface, an insertion depth of 1-2 mm beneath the tissue's suface, and an inserted fiber length of 1-2 cm. The syringe was mounted in an NE-500 syringe pump (New Era Pump Systems, Inc., Farmingdale, NY), and the flow rate was set to 50 µL/min. Infusion was conducted for 15 minutes for a total infused volume of 750 µL. Images were captured with an SLR camera (Canon USA, Lake Success, NY) every 30 seconds starting as the syringe pump was activated. The SWNH dispersal was traced and measured using ImageJ (NIH, Bethesda, MD) by two independent observers. Any area measurements with deviation greater than 10% were re-measured by a third observer. These experiments were conducted on two *ex vivo* bladders with a total of four injections.

c) Dispersal of Infused SWNHs throughout the Bladder's Layers

Experiments to determine the dispersal of SWNH solution through the thickness of the bladder wall were performed by infusing SWNHs into both inflated and uninflated healthy, *ex vivo* bladders. The *ex vivo* bladders used in these experiments were harvested from healthy, adult, mixed breed pigs of both sexes approximately 7 months in age from a regional abattoir (Smithsfield Foods, Inc., Smithsfield, VA). An uninflated bladder was bisected from the urethra to apex and pinned open with the urothelium displayed as shown in Figure 6. A set of infusions was made in the thin-walled tissue near the neck of the first bladder, where the needle was introduced through the urothelium at an angle of approximately 10° to a superficial depth (> 1

mm). These infusions were made at a flow rate of 50 µL/min for 5, 10, and 15 minutes. A second set of infusions was administered in a thicker-walled section near the apex of the bladder. The HCF was introduced at the same angle, but to a deeper penetration depth (2-4 mm) near the interface of the mucosa and muscularis propria. Infusions were conducted at a flow rate of 100 µL/min for 5, 10, and 15 minutes.

Following the completion of both sets of infusions, the bladder tissue was attached to a styrofoam sheet and immediately submerged in 10% neutral buffered formalin solution for fixation. Following a minimum of 24 hours of fixation, tissues were removed and trimmed for further processing. Tissues were dehydrated in a graded series of aqueous ethanols of increasing ethanol concentration, transitioned to ethanol/xylene, xylene/paraffin, and finally paraffin polymer. These dehydration and embedding procedures were done by a Tissue Tek® VIP® 6 automated tissue processing system (Sakura Finetek USA, Inc., Torrance, CA). Once infiltrated with paraffin polymer, three micron sections were cut, rehydrated, and then stained with hematoxylin-eosin stain, using an automated tissue stainer (Leica Microsystems, Wetzlar, Germany).

A third set of infusions was conducted near the apex of an inflated bladder. The HCF fiber was inserted at the same angle as above into the serosa of the bladder to a depth of 2-3 mm. Three infusions were administered at 50 µL/min for 5, 10, and 15 minutes, respectively. Immediately after the set of infusions was completed, the bladder was drained, the infused region excised, and the removed tissue attached to a styrofoam sheet for submersion in 10% neutral buffered

formalin solution. Following a minimum of 24 hours of fixation, tissues were removed and cut into thin, cross-sectional strips before being photographed with an SLR camera.

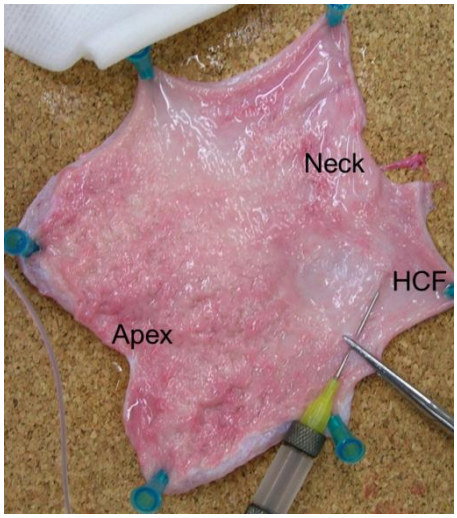

Figure 6: Experimental setup for FMD infusion of SWNHs into an isolated porcine bladder. Bladder has been bisected with the urothelium exposed. The HCF is inserted beneath the urothelial surface.

d) Laser Irradiation of Infused SWNHs

Experiments were conducted to test laser heating of infused SWNHs in the bladder wall using a 1064 nm CW diode-pumped fiber laser (IPG Photonics, Oxford, MA). The first experimental set was designed to determine the heating differences produced by laser irradiation of a SWNH perfused area of the bladder wall versus a non-infused control. A laser handpiece, delivering a collimated beam with a 5 mm beam width was used to irradiate the surface of the inflated bladder's serosal layer. Laser energy was delivered at an irradiance of 0.95 W/cm^2 for 40 seconds. Irradiation of the SWNH perfused tissue was conducted at the center of the visually detectable perfused area. Irradiation of the non-infused tissue was conducted at a similar anatomical location on the bladder wall approximately 1 cm away from the edge of the

distinguishable nanoparticle perfused region. During irradiation, thermographs of the temperature distribution across the bladder's surface were recorded at 60 Hz by an A40 Thermovision infrared thermal camera (FLIR Systems, Wilsonville, OR).

To determine whether the SWNHs efficacy as exogenous chromophores was independent of the Gaussian distribution of the laser beam, experiments were performed with a 1.5 cm beam width offset from the SWNH perfused bladder tissue. The *ex vivo* bladder was inflated and infused with SWNHs as described previously. The 5 mm collimated laser beam was expanded to a 1.5 cm beam width using an achromatic doublet lens (ThorLabs, Sterling, VA). The laser beam spot was offset from the discernibly perfused tissue such that only a portion of the beam's periphery was irradiating that tissue. The laser irradiance was 1.1 W/cm^2, and thermographs were taken over 40 seconds of laser heating.

e) Fiberoptic Microneedle Device Design Concept

Previous publications have described the FMD's evolving state of development, which has progressed to the current prototype incorporating a HCF capable of delivering both fluids and light [49-51]. A concept depiction of this design is shown in Figure 7. The HCF is commercially available light-guiding silica capillary tubing (365 µm outer diameter, 150 µm inner diameter, Polymicro Technologies, Phoenix, AZ) angle-polished at the tip to produce a sharp, beveled microneedle, shown in Figure 8. Light conduction is achieved by the principle of total internal reflection within the fused silica annular core (291 µm OD, n = 1.46) by having an exterior cladding layer of doped silica (15 µm OD, n= 1.44) and a fluid medium with a lower refractive index inside the inner bore [52].

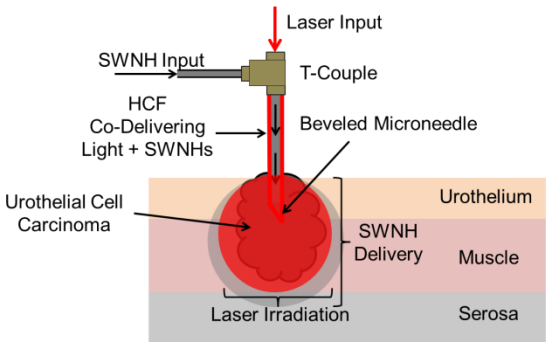

Figure 7: FMD design concept for bladder treatment. Light-guiding HCFs permit simultaneous co-delivery of laser light and fluid agents, enabling a combinatorial treatment.

To fabricate a prototype capable of co-delivery, the HCF was coupled with both a solid-core fiberoptic (80 µm outer diameter, 50 µm core diameter, Polymicro Technologies, Phoenix, AZ) and a 30 gauge syringe needle (Becton, Dickinson, Franklin Lakes, NJ) inside a 410 µm inner bore sheath made from a 22 gauge dispensing needle (McMaster-Carr, Atlanta, GA). A schematic of this co-delivery couple is shown in Figure 9. Light from a 1064 nm laser was coupled into the 80 µm solid-core fiber using a free space to fiberoptic coupler (Newport Corporation, Irvine, CA). The distal end of the fiber was placed inside a 22 gauge sheath (approximately 1 cm long) simultaneously with a 30 gauge syringe needle. Once the fiber and 30 gauge needle were positioned, epoxy (Master Bond Inc., Hackensack, NJ) was applied to the end of the sheath to hold them in place. The hollow-core fiber was aligned relative to the 80 µm fiber with a three-dimensional goniometer micropositioning stage (Opto Sigma, Santa Ana, CA). Coupling efficiency was determined by placing the distal end of the hollow-core fiber into an integrating sphere (Newport Corporation, Irvine, CA). Once a coupling efficiency of >30% was

attained, the hollow-core fiber was also epoxied into the sheath. Both ends of the sheath were epoxied a second time to ensure a robust fluid seal.

Figure 8: Image of beveled microneedle at the tip of a HCF. Water is visible inside the hollow bore.

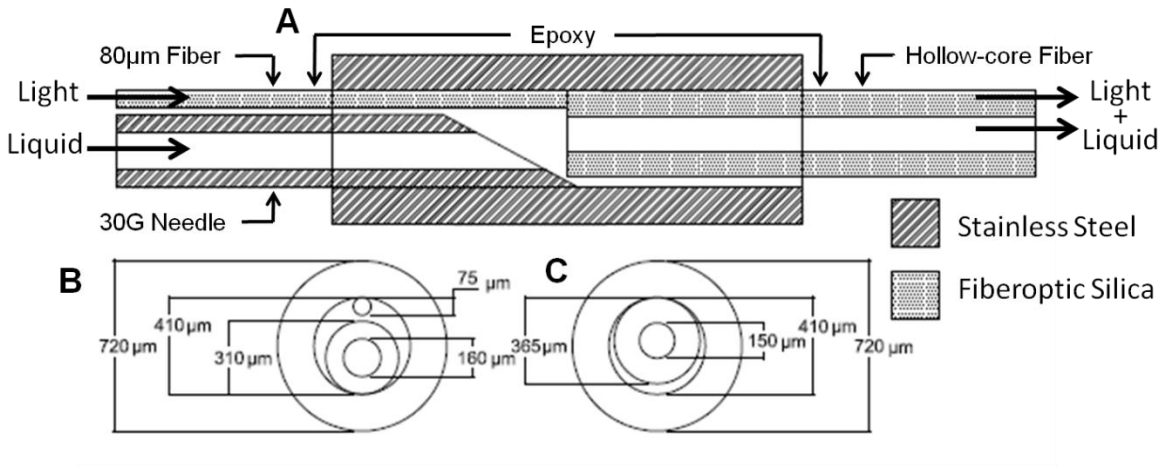

Figure 9: Schematic of FMD co-delivery couple design. A) Cut-away of the co-delivery couple showing the alignment of the light conducting fibers and position of the fluid input, B) cross-section of the input of the couple, exhibiting the position of the light and fluid inputs, and C) cross-section of the output of the couple, exhibiting the position of the co-delivery HCF.

f) Demonstration of Co-Delivery with a Fiberoptic Microneedle Device

Experiments demonstrating co-delivery through a single HCF were performed through sequential delivery of SWNH solution and laser light into healthy, *ex vivo* bladders. Light from a 1064 nm laser was coupled into an 80 μm solid-core fiber using a free space to fiberoptic coupler. A 30 gauge needle fluid input was attached to a syringe filled with a 0.05 mg/mL SWNH solution. Pressurized flow was provided by an NE-500 syringe pump. The distal end of the co-delivery HCF was introduced into the wall of an inflated, *ex vivo* bladder (as described previously). HCFs were manually inserted at an angle of approximately 10° through the serosa of the inflated bladder. Insertion depths and inserted lengths varied between 1-2 mm and 1-2 cm, respectively. Infusion was conducted at 20 μL/min for 25 min, and the expanding nanoparticle perfused area was captured every 1 min with an SLR camera. After infusion was complete, the sample was irradiated with 1064 nm laser light conducted through a HCF at 400 W/cm^2 for 40 seconds. A control experiment irradiating a non-infused bladder wall with the same power was also performed. Thermographs of the irradiated tissue were captured via IR thermography as described previously.

3.4 Results

a) Dispersal of SWNHs Across the Serosa of the Bladder

The silica HCFs were sufficiently robust to be inserted into the inflated, *ex vivo* bladder wall's serosa and muscularis numerous times without incurring breakage or breaching the bladder wall by overpenetration into the lumen. A representative series of time lapse images are shown below in Figure 10.

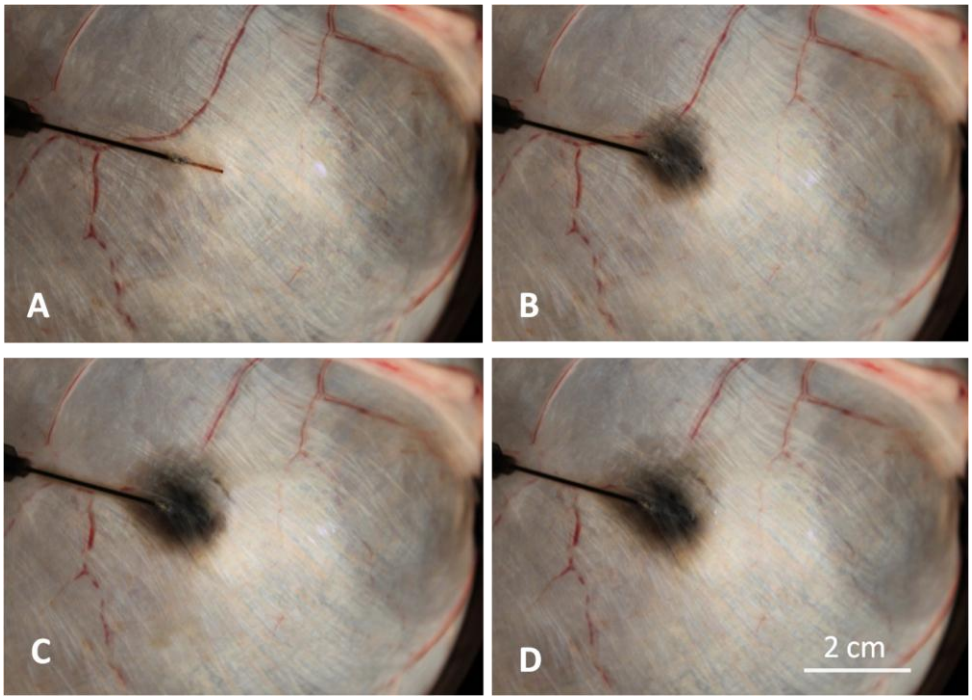

Figure 10: SWNH infusion through HCF into an *ex vivo* porcine bladder wall. A) t = 0, area = 0 B) t = 4 min, area = 1.5 cm^2 C) t = 8 min, area = 2.6 cm^2 D) t = 12 min, 3.2 cm^2

SWNH area expansion across the serosa was shown to increase at a relatively linear average rate of 0.36 ± 0.08 cm^2/min when infused at 50 µL/min. A graph of the average values across the 15 min experiments is shown below in Figure 11.

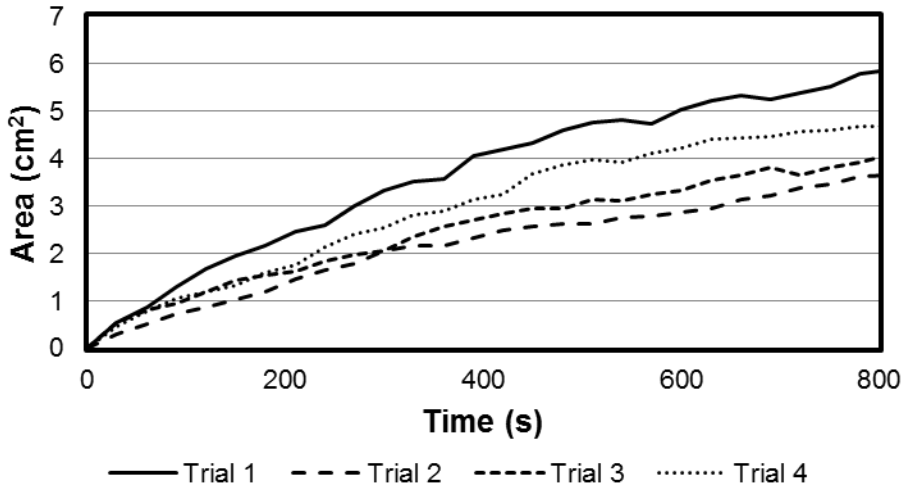

Figure 11: Area versus time plot of data from the SWNH infusions into inflated bladders.

b) Dispersal of Infused SWNHs throughout the Bladder's Layers

HCFs were placed into the urothelium of the bisected bladder without sustaining any damage. Reflux of fluid escaping the interstitial space by traveling along the fiber's length was dependent on flow rate. Infusions at 50 µL/min produced little to no reflux, while infusions at 100 µL/min caused obvious bolus formation and some reflux. A photograph of the first two sets of infusion is shown in Figure 12. Formalin-fixed gross sections exhibited SWNH dispersal throughout the thickness of the tissue for each of the infusions near the neck of the bladder. Similar sections in thicker tissue near the bladder's apex showed SWNH dispersal through 4-5 mm of the wall's thickness. SWNH dispersal in the stained sections was evident by the expansion of the mucosal layer, which correlated highly with the localization of nanoparticles evident in the gross section from the thicker tissue shown in Figure 13.

Fixed cross-sections from the infusion sites into the inflated bladder unanimously exhibited SWNH penetration throughout the thickness of the wall. A representative photograph is shown in Figure 13.

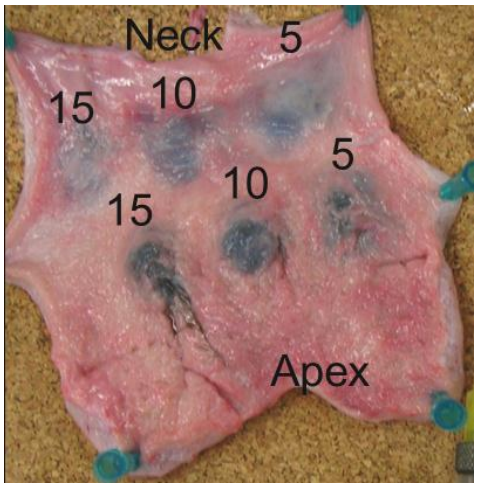

Figure 12: Two sets of infusions, located proximal to the neck and apex of the bladder, respectively, are labeled with their infusion times in minutes. The infusion rate was 50 µL/min for the neck infusions and 100 µL/min for the apical infusions.

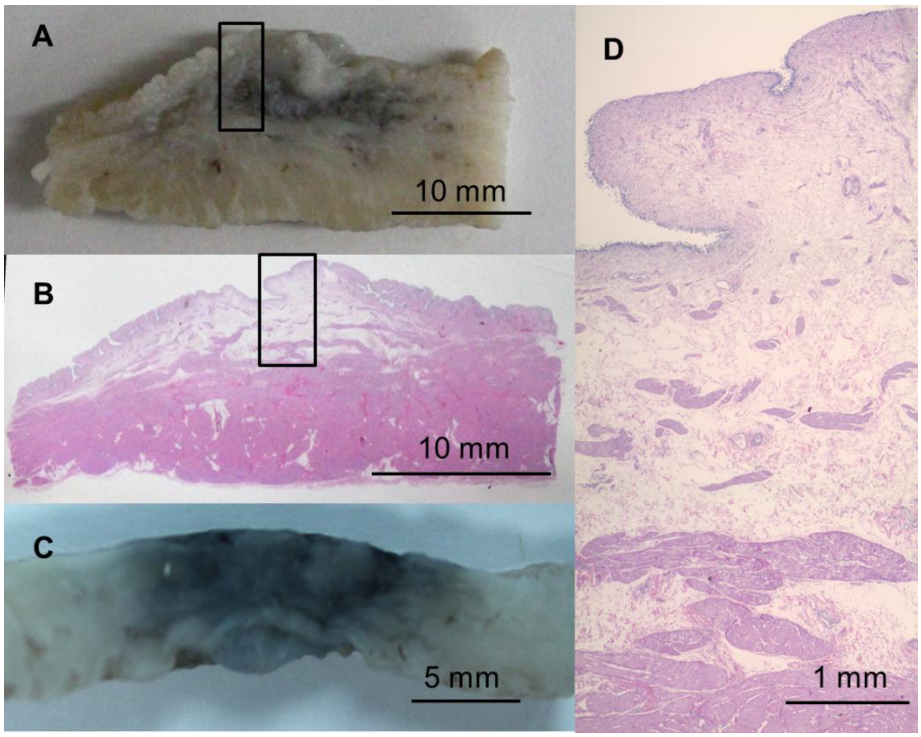

Figure 13: (A) Gross section fixed bladder wall following 5 minute infusion into thicker/apical region of uninflated bladder (B) Histological section cut directly from the gross section (A). (C) Gross section of fixed bladder wall following 10 minute infusion into inflated bladder (D) Close view of the stained section (location denoted by black boxes in (A) and (B)) showing expansion of the loose connective tissue in the mucosal layer from fluid expansion caused by SWNH infusion.

c) Laser Irradiation of Infused SWNHs

The temperature increase of an inflated, *ex vivo* bladder wall irradiated with 1064 nm laser energy (0.95 W/cm^2) was measured at a region infused with SWNHs and a control region without infusion. Laser heating of a non-infused area yielded a temperature increase of approximately 5 °C, while the heating of a SWNH infused area had a temperature increase of approximately 24 °C. Thermographs of these results are shown in Figure 14.

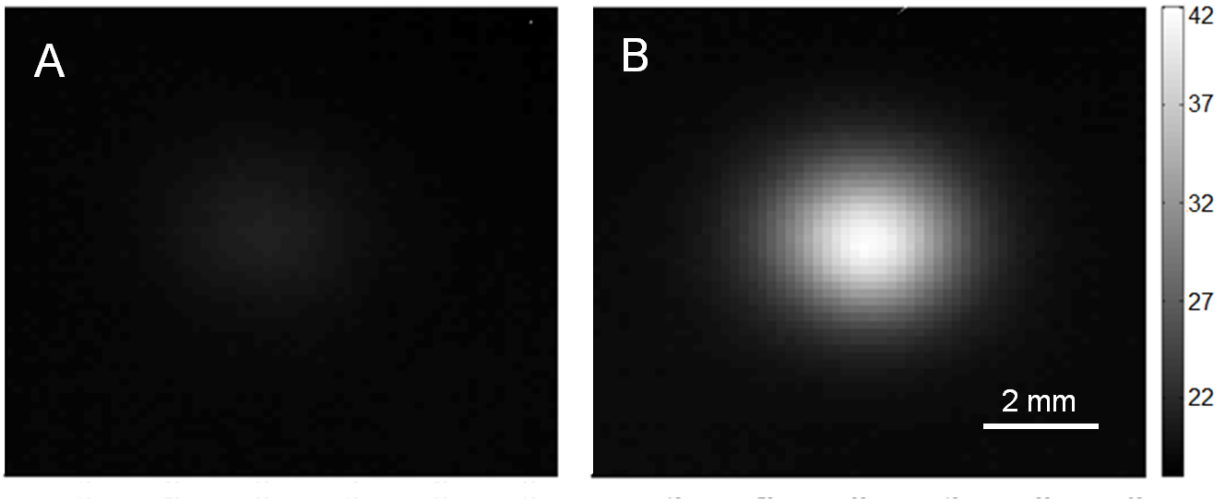

Figure 14: Thermographs of laser heating perfused bladder tissue in regions: (A) without SWNHs and (B) with SWNHs. The color scale depicts temperature in Celsius.

Experiments utilizing an offset laser spot to heat the edge of the SWNH perfused tissue demonstrated that the significant difference in heating caused by the exogenous chromophores was independent of the Gaussian profile of the laser beam. A representative thermograph of the offset laser spot heating at an irradiance of 1.1 W/cm^2 for 40 seconds is shown in Figure 15. A detectable temperature gradient was observed across the laser spot on the tissue correlating with the position of the nanoparticle spot.

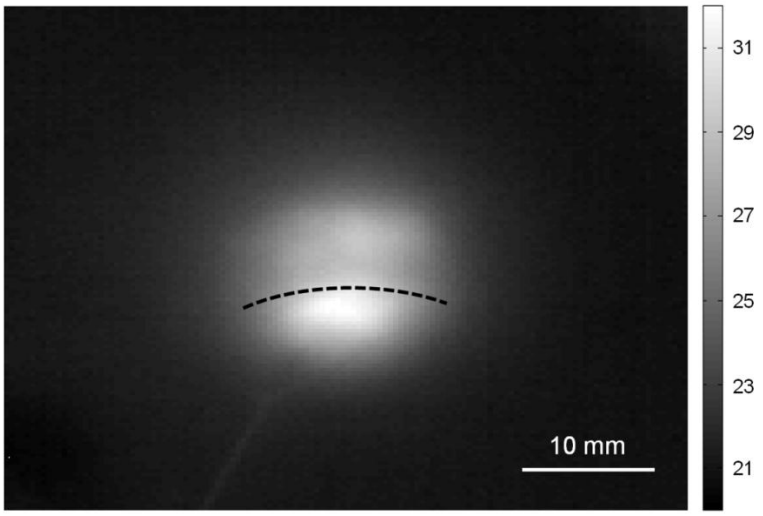

Figure 15: Thermograph of laser irradiation on SWNH perfused bladder wall with a 1.5 cm beam width. The highest temperature correlates with the laser/SWNH overlap. The dotted line marks the top edge of the SWNH spread. Color scale is in Celsius.

d) Demonstration of Co-Delivery with Fiberoptic Microneedle Device

The co-delivery couple prototype had a light coupling efficiency of 35% between an 80 μm solid-core fiber and a HCF. Experiments demonstrating the feasibility of co-delivery through a single HCF exhibited a maximum temperature increase of 33 °C when irradiated at 400 W/cm^2 for 40 seconds. Temperature increase for non-perfused tissue at the same irradiance and time was 5 °C. Representative images of the light delivery to both infused and non-infused regions of the bladder wall are shown in Figure 16.

Figure 16: Irradiation from light-guiding, hollow-core microneedle after delivering SWNHs into the inflated bladder wall. (A) photograph showing microneedle position (Note: the red guide laser is visible), (B) thermograph of non-infused control, and C) thermograph of SWNH perfused tissue. Color scale is in Celsius, white lines denote fiber path.

3.5 Discussion

The experiments performed in this study demonstrated the feasibility of treating invasive UCCs with the FMD through co-delivery of SWNHs and 1064 nm laser energy into healthy, *ex vivo* bladders. Experimental results indicated that the SWNHs can be readily delivered into the interstitial space through the HCFs, with significant expansion across the bladder wall and through the entirety of the wall's thickness. Laser irradiation of the infused SWNHs exhibited significantly increased heating in comparison to non-infused tissue. The FMD's ability to successfully co-deliver SWNH solution and laser irradiation sequentially through a single HCF was demonstrated.

SWNHs offer several advantages over alternative exogenous chromophores that could be used with the FMD. One of the most important advantages over other nanoparticles is that SWNHs

are produced without the use of metal catalysts, significantly lowering their cytotoxicity; this is a desirable trait, as infused SWNH would not be expected to damage normal bladder cellularity when used to treat tumors [47, 53, 54]. Future *in vivo* studies to determine how SWNHs are expelled from the bladder tissue will be conducted. While this paper focused on the photothermal heating aspect, SWNHs have been demonstrated to produce reactive oxygen species when heated. This implies that the proposed treatment regimen will produce both photothermal and photochemical injury in tumors [55, 56]. In addition, SWNHs have been functionalized in several different studies with image-enhancing tags, cell targeting moieties, and photo-activated drugs, emphasizing their role as a versatile tool that can be altered for specific applications [47, 56-67].

Experiments to determine the dispersal of SWNHs along the bladder wall utilized healthy bladders excised from freshly sacrificed research animals. As a result, the bladders closely resembled normal tissues in both structure and biomechanical properties. The primary difference between the *ex vivo* tissue used and a normal, intact bladder case was the lack of blood perfusion within the tissue. Blood perfusion may increase rate of dispersal of SWNHs through the bladder's interstitial space while pulling some of the particles into the systemic circulation, perhaps lowering effective concentration in a target UCC. A large invasive UCC can be defined as being >1 cm in diameter (assuming a roughly spherical geometry) [34]. This suggests that the largest tumors likely to be treated with this device could be assumed to have an observable surface manifestation on the bladder wall between 1-2 cm^2. If the rate of SWNH area expansion measured in this study would be conserved in the *in vivo* case, FMD infusion of SWNHs should penetrate this large tumor within approximately 5 minutes at a volumetric flow rate of 50

μL/min. However, further experimentation in an *in vivo* model would be needed to fully test this conclusion.

The experiments determining dispersal of infused SWNHs through the bladder's layers demonstrated penetration throughout the thickness of bladder walls less than 5 mm in depth after 5 minutes of infusion at 50 μL/m. However, this finding was not observed for thicker regions (average thickness ~9 mm) of the bladder wall at the apex of the uninflated bladder, which exhibited SWNH dispersal primarily confined to the urothelial and mucosal layers. This suggests that the more substantial muscular layer in the thicker sample was less permeable to the SWNH solution. As thickening of the muscular layer results from the death of the animal model, bladders in living patients should more closely resemble the thin-wall case.

The detectable footprint of infused SWNHs was roughly circular for all the experiments (as shown in Figure 11). The center of this circle was at the midlength of the hollow-core microneedle's protrusion from the 22 gauge syringe needle, as opposed to the beveled microneedle tip. Reflux along the shaft of an infusion needle is typically observed in applications such as convection-enhanced delivery (CED) [68]. Krauze et al. proposed an improvement in CED infusion cannula designs through inclusion of a step change increase in needle diameter some distance from the cannula's tip, which was shown to halt the progression of reflux [69]. That design is mimicked in our FMD for the bladder tissue, and a similar effect of the reflux stopping at the 22 gauge needle was observed. Once the fluid pocket of reflux around the HCF portion of the design stabilized, the fluid pushed out into the surrounding bladder tissue, resulting in the roughly circular footprint with a centerpoint at the midlength of the silica shaft.

Laser irradiation of SWNH perfused tissue with a free space laser exhibited the efficacy of the nanoparticles as exogenous chromophores within the bladder wall. The maximum heating difference between irradiating perfused and non-perfused tissue was approximately 480%. For many hyperthermic therapies, the heating threshold for quickly causing protein denaturation and tissue coagulation beyond reversible damage has been shown to be 60 °C [28, 70]. The maximum tissue temperature increase in the SWNH-perfused tissue was approximately 24 °C, a shift from physiological temperature (37 °C) past this therapeutic target. More heating could be obtained by either increasing the laser irradiance or raising the local concentration of nanoparticles [47, 48]. The substantial heating increase demonstrated that SWNHs can aid laser heating of tissue in reaching temperatures inducing rapid hyperthermic tissue damage.

The offset laser spot experiment demonstrated that the increase in heating due to SWNH absorption was independent of the laser beam's Gaussian profile, but more importantly it demonstrated that heating correlated with the infused region of SWNHs. This implies that by utilizing the HCF's ability to penetrate the bladder wall, SWNHs can be delivered to shape the zone of photothermal heating from within deeper bladder layers containing neoplastic tissue. This fulfills an objective of the FMD technology, which is not simply attaining higher temperatures, but creating a temperature distribution that can be shaped to specifically target invasive UCCs. This experiment provides evidence that if the SWNH distribution can be contained within a target volume, laser irradiation should cause selective tissue destruction while preserving healthy tissue.

The experiments utilizing the HCF for both the fluid and light delivery demonstrated proof of concept for the FMD. Successful infusion of SWNH solution followed by 1064 nm laser light irradiation heated tissue to a maximum temperature shift of 33 °C within 40 seconds of heating the tissue at 400 W/cm^2. Optimization of treatment parameters and approach were not an objective of this pilot study, as the *in vivo* case may differ from the tissue utilized. Although the volume treatable by a single cycle of co-delivery may prove insufficient for photocoagulation of a target tumor's margins, multiple heating cycles, insertions, or fibers in parallel could be utilized to increase the treated volume and efficacy of treatment. These results substantiate the feasibility of selective photothermal treatment at invasive tumor depths with the FMD.

The FMD can potentially deliver a variety of different laser wavelengths, fluids, and drugs in addition to the specific parameters used in this study. Ho:YAG lasers (2.1 μm) have become a widely used alternative to TURB for treatment of superficial bladder tumors, and Tm:YAG (~2 μm) has been shown to be similarly efficacious [35]. Co-delivery couples could be made for either of these wavelengths, allowing clinicians a choice for specific cases. However, the use of these wavelengths would render the SWNHs inconsequential as they are highly absorbed by water, and the specificity of the treatment would be dependent on the interstitial position of the microneedle tip. The fluid delivery modality could alternatively be used to deliver adjunctive, local treatments such as chemotherapy. This versatile, enabling technology can be useful for a wide variety of treatment options in addition to the therapeutic concept outlined in the above experiments.

3.7 Conclusion

This study develops a novel microneedle-based method and device for potentially treating invasive UCCs. The device utilizes a light-guiding, HCF (150 µm inner bore, 365 µm outer diameter), angle-polished to obtain a beveled microneedle tip. Experiments investigating the fluid dispersal of SWNHs in the wall of inflated, *ex vivo* bladders demonstrated that an area coverage of 2 cm^2 on the bladder wall's surface can be achieved with a 5 minute infusion at 50 µL/min. SWNH infusion into inflated bladders exhibited dispersal throughout the thickness of a 5 mm bladder wall after a 5 minute infusion at 50 µL/min. Irradiation of the SWNH perfused bladder wall tissue for 40 seconds at 0.95 W/cm^2 with 1064 nm laser light yielded a 480% temperature increase relative to similar irradiation of a non-infused control. Proof of concept experiments demonstrated both SWNH and light delivery though a single HCF to heat the bladder wall 33 °C by laser irradiation at 400 W/cm^2 for 40 seconds. This demonstrated the feasibility of utilizing the FMD to achieve hyperthermia-based therapeutic effects via interstitial irradiation. In clinical applications, the proposed design would integrate the microneedle with a commercial cystoscope. The composite device is envisioned to be introduced into the bladder's lumen, where the HCF will be mechanically actuated to penetrate into the bladder wall's interstitial space. Once placed, the microneedle will be used to deliver photoabsorbing SWNHs and 1064 nm laser light to photothermally induce hyperthermic cell death.

Chapter 4: **Conclusions**

4.1 Summary

The two studies above described the hydraulic resistance characterization of hollow-core fiberoptic microneedles and the development of the FMD for treating invasive bladder cancer. They outline the design progress of the fluid-delivering FMD from basic science to development for a clinical application. The work represented was a demonstration of the engineering advantages the FMD offers as a therapeutic device: tissue penetration to interstitial space, fluid delivery, and light delivery.

The first study investigated the fluid flow properties through light-guiding, hollow-core fiber (365 μm OD, 150 μm ID) by measuring the volumetric flow rate through the fiber at different input pressures. Experiments were conducted on both straight tubing and fibers with tapering microneedle tips fabricated through our novel melt-drawing technique. Collected data was compared to theoretically predicted values from Poiseuille's Law. The findings from the study were incorporated into the next design permutations of the FMD.

The second study described the design and development of the co-delivery aspect of the FMD. Fabrication of a novel co-delivery device for coupling fluids and light into a single, hollow-core fiber was described. SWNHs were investigated as novel photoabsorbers for the localization of

photothermal heating in bladder cancer. Experiments demonstrating proof of the FMD's potential as a bladder cancer treatment by delivery of SWNHs in solution and 1064 nm laser light to achieve heating of *ex vivo* bladder tissue to levels of irreversible hyperthermic cell damage were described and analyzed.

4.2 Conclusions

The hydraulic resistance characterization manuscript chronicles the early development of the hollow-core FMD. The study determined that for straight tubing with an inner bore of 150 µm and a length greater than 50 mm long, Poiseuille's Law was shown to be accurate within 12% of experimental data for the pressure range of 69-517 kPa. This silica tubing was also shown to have similar hydraulic resistance to microneedles fabricated from the tubing through our proprietary method. Comparison between different needle design geometries indicated that tip diameters <55 µm cause a significant increase in hydraulic resistance. Tubing length should be kept to a minimum and tip diameter should be kept above this threshold to reduce overall hydraulic resistance.

This study develops a novel microneedle-based method and device for potentially treating invasive UCCs. The device utilizes a light-guiding, HCF (150 µm inner bore, 365 µm outer diameter), angle-polished to obtain a beveled microneedle tip. Experiments investigating the fluid dispersal of SWNHs in the wall of inflated, *ex vivo* bladders demonstrated that an area coverage of 2 cm^2 on the bladder wall's surface can be achieved with a 5 minute infusion at 50 µL/min. SWNH infusion into inflated bladders exhibited dispersal throughout the thickness of a 5 mm bladder wall after a 5 minute infusion at 50 µL/min. Irradiation of the SWNH perfused bladder wall tissue for 40 seconds at 0.95 W/cm^2 with 1064 nm laser light yielded a 480%

temperature increase relative to similar irradiation of a non-infused control. Proof of concept experiments demonstrated both SWNH and light delivery though a single HCF to heat the bladder wall 33 °C by laser irradiation at 400 W/cm^2 for 40 seconds. This demonstrated the feasibility of utilizing the FMD to achieve hyperthermia-based therapeutic effects via interstitial irradiation. In clinical applications, the proposed design would integrate the microneedle with a commercial cystoscope. The composite device is envisioned to be introduced into the bladder's lumen, where the HCF will be mechanically actuated to penetrate into the bladder wall's interstitial space. Once placed, the microneedle will be used to deliver photoabsorbing SWNHs and 1064 nm laser light to photothermally induce hyperthermic cell death.

Chapter 5: **References**

1. Kaushik, S., et al., *Lack of pain associated with microfabricated microneedles.* Anesth Analg, 2001. **92**(2): p. 502-4.
2. Gill, H.S., et al., *Effect of microneedle design on pain in human volunteers.* Clin J Pain, 2008. **24**(7): p. 585-94.
3. Gill, H.S. and M.R. Prausnitz, *Does needle size matter?* J Diabetes Sci Technol, 2007. **1**(5): p. 725-9.
4. Cormier, M., et al., *Transdermal delivery of desmopressin using a coated microneedle array patch system.* J Control Release, 2004. **97**(3): p. 503-11.
5. Liu, R., X. Wang, and Z. Zhou, *[Application of MEMS microneedles array in biomedicine].* Sheng Wu Yi Xue Gong Cheng Xue Za Zhi, 2004. **21**(3): p. 482-5.
6. Mukerjee, E.V., et al., *Microneedle array for measuring wound generated electric fields.* Conf Proc IEEE Eng Med Biol Soc, 2006. **1**: p. 4326-8.
7. Yan, K., H. Todo, and K. Sugibayashi, *Transdermal drug delivery by in-skin electroporation using a microneedle array.* Int J Pharm, 2010.
8. Jiang, J., et al., *Intrascleral drug delivery to the eye using hollow microneedles.* Pharmaceutical Research, 2009. **26**(2): p. 395-403.
9. Prausnitz, M.R., et al., *Microneedle-based vaccines.* Curr Top Microbiol Immunol, 2009. **333**: p. 369-93.
10. Park, J.H., M.G. Allen, and M.R. Prausnitz, *Polymer microneedles for controlled-release drug delivery.* Pharmaceutical Research, 2006. **23**(5): p. 1008-19.
11. Park, J.H., M.G. Allen, and M.R. Prausnitz, *Biodegradable polymer microneedles: fabrication, mechanics and transdermal drug delivery.* J Control Release, 2005. **104**(1): p. 51-66.
12. Lee, J.W., J.H. Park, and M.R. Prausnitz, *Dissolving microneedles for transdermal drug delivery.* Biomaterials, 2008. **29**(13): p. 2113-24.
13. Davis, S.P., et al., *Hollow metal microneedles for insulin delivery to diabetic rats.* IEEE Trans Biomed Eng, 2005. **52**(5): p. 909-15.
14. Martanto, W., et al., *Transdermal delivery of insulin using microneedles in vivo.* Pharmaceutical Research, 2004. **21**(6): p. 947-52.
15. Roxhed, N., et al., *Painless drug delivery through microneedle-based transdermal patches featuring active infusion.* IEEE Trans Biomed Eng, 2008. **55**(3): p. 1063-71.
16. *Bladder Cancer Overview*. Learn About Cancer 07/01/2010 [cited 2011 07/01/2011]; Available from: http://www.cancer.org/cancer/bladdercancer/overviewguide/bladder-cancer-overview-survival-rates.
17. Quek, M.L., et al., *Prognostic significance of lymphovascular invasion of bladder cancer treated with radical cystectomy.* J Urol, 2005. **174**(1): p. 103-6.
18. Wong-You-Cheong, J.J., et al., *From the archives of the AFIP - Neoplasms of the urinary bladder: Radiologic-pathologic correlation.* Radiographics, 2006. **26**(2): p. 553-U17.
19. *Bladder Cancer*. [cited 2011 07/08/2011]; Available from: http://uvahealth.com/services/cancer-center/conditions-treatments/12015.
20. Rodel, C., et al., *Combined-modality treatment and selective organ preservation in invasive bladder cancer: Long-term results.* Journal of Clinical Oncology, 2002. **20**(14): p. 3061-3071.
21. *Bladder Cancer Treatment*. 2009 8/21/2009 [cited 2010; Available from: http://www.cancer.gov/cancertopics/pdq/treatment/bladder/Patient/page4.
22. Thrasher, J.B. and E.D. Crawford, *Current management of invasive and metastatic transitional cell carcinoma of the bladder.* J Urol, 1993. **149**(5): p. 957-72.

23. Hart, S., et al., *Quality of life after radical cystectomy for bladder cancer in patients with an ileal conduit, cutaneous or urethral kock pouch.* The Journal of urology, 1999. **162**(1): p. 77-81.
24. Stein, J.P., et al., *Radical cystectomy in the treatment of invasive bladder cancer: long-term results in 1,054 patients.* Journal of clinical oncology : official journal of the American Society of Clinical Oncology, 2001. **19**(3): p. 666-75.
25. Syed, H.A., et al., *Holmium : YAG laser treatment of recurrent superficial bladder carcinoma: Initial clinical experience.* Journal of Endourology, 2001. **15**(6): p. 625-627.
26. Larizgoitia, I. and J.M.V. Pons, *A systematic review of the clinical efficacy and effectiveness of the holmium : YAG laser in urology.* Bju International, 1999. **84**(1): p. 1-9.
27. Soler-Martinez, J., et al., *Holmium laser treatment for low grade, low stage, Noninvasive bladder cancer with local anesthesia and early instillation of mitomycin C.* Journal of Urology, 2007. **178**(6): p. 2337-2339.
28. Pietrow, P.K. and J.A. Smith, Jr., *Laser treatment for invasive and noninvasive carcinoma of the bladder.* Journal of endourology / Endourological Society, 2001. **15**(4): p. 415-8; discussion 425-6.
29. Hruby, G.W., et al., *Transurethral bladder cryoablation in the porcine model.* Journal of Urology, 2008. **179**(4): p. 365-365.
30. Sternberg, C.N., et al., *Chemotherapy for bladder cancer: treatment guidelines for neoadjuvant chemotherapy, bladder preservation, adjuvant chemotherapy, and metastatic cancer.* Urology, 2007. **69**(1 Suppl): p. 62-79.
31. Malkowicz, S.B., et al., *Muscle-invasive urothelial carcinoma of the bladder.* Urology, 2007. **69**(1 Suppl): p. 3-16.
32. Fedeli, U., S.A. Fedewa, and E.M. Ward, *Treatment of muscle invasive bladder cancer: evidence from the National Cancer Database, 2003 to 2007.* The Journal of urology, 2011. **185**(1): p. 72-8.
33. Kramer, M.W., et al., *Current evidence for transurethral laser therapy of non-muscle invasive bladder cancer.* World J Urol, 2011.
34. Johnson, D.E., *Use of the Holmium-Yag (Ho Yag) Laser for Treatment of Superficial Bladder-Carcinoma.* Lasers in Surgery and Medicine, 1994. **14**(3): p. 213-218.
35. Kramer, M.W., et al., *Current evidence for transurethral laser therapy of non-muscle invasive bladder cancer.* World journal of urology, 2011.
36. Das, A., P. Gilling, and M. Fraundorfer, *Holmium laser resection of bladder tumors (HoLRBT).* Techniques in urology, 1998. **4**(1): p. 12-4.
37. Ghoneim, M.A., et al., *Radical cystectomy for carcinoma of the bladder: critical evaluation of the results in 1,026 cases.* The Journal of urology, 1997. **158**(2): p. 393-9.
38. Kosoglu, M., et al., *Fiberoptic Microneedles for Transdermal Light Delivery: Ex Vivo Porcine Skin Penetration Experiments.* Journal of Biomechanical Engineering, 2010. **132**(9): p. 091014:1-7.
39. Ramasubramanian, M.K., O.M. Barham, and V. Swaminathan, *Mechanics of a mosquito bite with applications to microneedle design.* Bioinspir Biomim, 2008. **3**(4): p. 046001.
40. Kirby, B., *Micro- and nanoscale fluid mechanics : transport in microfluidic devices*2010, New York: Cambridge University Press. xxiii, 512 p.
41. Munson, B.R. and T.H. Okiishi, *Fundamentals of fluid mechanics*. 6th ed2009, Hoboken, NJ: J. Wiley & Sons. 1 v. (various pagings).
42. Incropera, F.P., *Fundamentals of heat and mass transfer*. 6th ed2007, Hoboken, NJ: John Wiley. xxv, 997 p.
43. Zahn, J.D., et al., Biomedical Microdevices, 2000. **2**(4): p. 295-303.
44. Sutterby, J., *Laminar Newtonian and Non-Newtonian Converging Flow in Conical Sections*, in *PhD Dissertation*1964, University of Wisconsin: Madison, WI.

45. Jarzebski, A.B. and W.L. Wilkinson, *Non-Isothermal Developing Flow of a Generalized Power-Law Fluid in a Tapered Tube.* Journal of Non-Newtonian Fluid Mechanics, 1981. **8**(3-4): p. 239-248.
46. Cheng, M.D., et al., *Formation studies and controlled production of carbon nanohorns using continuous in situ characterization techniques.* Nanotechnology, 2007. **18**(18).
47. Whitney, J.R., et al., *Single Walled Carbon Nanohorns as Photothermal Cancer Agents.* Lasers in Surgery and Medicine, 2011. **43**(1): p. 43-51.
48. Sarkar, S., et al., *Optical properties of breast tumor phantoms containing carbon nanotubes and nanohorns.* Journal of biomedical optics, 2011. **16**(5): p. 051304.
49. Hood, R.L., Kosoglu, M.A., Parker, M., Rylander, C.G., *Effects of Microneedle Design Parameters on Hydraulic Resistance.* ASME Journal of Medical Devices: p. In Revision.
50. Kosoglu, M.A., Hood, R.L., Rossmeisl, J.H., Grant, D.C., Robertson, J.L., Rylander, M.N., Rylander, C.G., *Fiberoptic Microneedles: Novel Optical Diffusers for Interstitial Delivery of Therapeutic Light.* Lasers in surgery and medicine: p. In Revision.
51. Kosoglu, M.A., et al., *Fiber Optic Microneedles for Transdermal Light Delivery: Ex Vivo Porcine Skin Penetration Experiments.* Journal of Biomechanical Engineering-Transactions of the Asme, 2010. **132**(9): p. -.
52. DeGrandpre, M.D., et al., *Characterization of long pathlength capillary waveguides for evanescent fluorescence sensing applications.* Sensors and Actuators B-Chemical, 2008. **135**(1): p. 145-151.
53. Miyawaki, J., et al., *Toxicity of single-walled carbon nanohorns.* ACS nano, 2008. **2**(2): p. 213-26.
54. Murata, K., et al., *Molecular potential structures of heat-treated single-wall carbon nanohorn assemblies.* Journal of Physical Chemistry B, 2001. **105**(42): p. 10210-10216.
55. Whitney, J., et al., *Carbon Nanohorns as Photothermal and Photochemical Laser Cancer Therapeutic Agents.* Lasers in surgery and medicine, 2009: p. 3-3.
56. Miyako, E., et al., *Near-infrared laser-triggered carbon nanohorns for selective elimination of microbes.* Nanotechnology, 2007. **18**(47).
57. Miyawaki, J., et al., *Biodistribution and ultrastructural localization of single-walled carbon nanohorns determined in vivo with embedded Gd2O3 labels.* ACS nano, 2009. **3**(6): p. 1399-406.
58. Isobe, H., et al., *Preparation, purification, characterization, and cytotoxicity assessment of water-soluble, transition-metal-free carbon nanotube aggregates.* Angewandte Chemie, 2006. **45**(40): p. 6676-80.
59. Ajima, K., et al., *Effect of functional groups at hole edges on cisplatin release from inside single-wall carbon nanohorns.* The journal of physical chemistry. B, 2006. **110**(11): p. 5773-8.
60. Ajima, K., et al., *Optimum hole-opening condition for Cisplatin incorporation in single-wall carbon nanohorns and its release.* The journal of physical chemistry. B, 2006. **110**(39): p. 19097-9.
61. Murakami, T., et al., *Drug-loaded carbon nanohorns: adsorption and release of dexamethasone in vitro.* Molecular pharmaceutics, 2004. **1**(6): p. 399-405.
62. Ajima, K., et al., *Carbon nanohorns as anticancer drug carriers.* Molecular pharmaceutics, 2005. **2**(6): p. 475-80.
63. Murakami, T., et al., *Solubilization of single-wall carbon nanohorns using a PEG-doxorubicin conjugate.* Molecular pharmaceutics, 2006. **3**(4): p. 407-14.
64. Matsumura, S., et al., *Dispersion of cisplatin-loaded carbon nanohorns with a conjugate comprised of an artificial peptide aptamer and polyethylene glycol.* Molecular pharmaceutics, 2007. **4**(5): p. 723-9.
65. Kase, D., et al., *Affinity selection of peptide phage libraries against single-wall carbon nanohorns identifies a peptide aptamer with conformational variability.* Langmuir : the ACS journal of surfaces and colloids, 2004. **20**(20): p. 8939-41.

66. Sano, K., et al., *Endowing a ferritin-like cage protein with high affinity and selectivity for certain inorganic materials.* Small, 2005. **1**(8-9): p. 826-32.
67. Iijima, S., et al., *Nano-aggregates of single-walled graphitic carbon nano-horns.* Chemical Physics Letters, 1999. **309**(3-4): p. 165-170.
68. Morrison, P.F., et al., *Focal delivery during direct infusion to brain: role of flow rate, catheter diameter, and tissue mechanics.* The American journal of physiology, 1999. **277**(4 Pt 2): p. R1218-29.
69. Krauze, M.T., et al., *Reflux-free cannula for convection-enhanced high-speed delivery of therapeutic agents - Technical note.* Journal of Neurosurgery, 2005. **103**(5): p. 923-929.
70. Dowlatshahi, K., et al., *Stereotactically guided laser therapy of occult breast tumors: work-in-progress report.* Archives of surgery, 2000. **135**(11): p. 1345-52.

Appendix A: Annotated List of Figures